GEOPHYSICS, VOL. 91, NO. 4 (JULY-AUGUST 2026); P. KS73–KS87, 28 FIGS.
10.1190/GEO-2025-0270

Directional characteristic analysis of wavefields excited by high-speed train seismic sources

Xiaokai Wang[1], Shengpei Xia[1], Chuanli Xiao[1], Jingrui Luo[2], Wenchao Chen[1], Dawei Liu[1], Zhaodan Liu[3], and Ningning Zhou[1]

ABSTRACT

High-speed trains (HSTs) generate strong ground vibrations when running on railways, which excite stable seismic waves. As these seismic waves propagate through the subsurface medium, they carry valuable information about geologic structures, which can be effectively used for imaging and inversion. To fully use HST seismic data, it is crucial to understand and characterize the wavefield characteristics of the HST source. Using the theory of a uniform linear array, the directional characteristics of a seismic wavefield excited by HST sources were analyzed. Furthermore, using the ABAQUS finite element analysis software, a model depicting an HST traversing a tunnel was established. The simulation results of the HST seismic wavefield were used for theoretical verification. By comparing the theoretical radiation patterns of the HST seismic wavefield with those of the simulated wavefield, strong consistency between the main lobes of the interference patterns was observed. Notably, this conclusion remained valid even when the HST speed or medium parameters were changed.

INTRODUCTION

Recently, demand for long-distance travel has increased significantly, leading to the rapid development of high-speed trains (HSTs). Owing to the prohibition of traditional active seismic sources along high-speed railways (HSR), the imaging of underground structures in these areas lacks effective seismic sources. Given the characteristics of HSTs, such as similar structures, fast and stable running speeds, and dense railway networks, HST sources have become green, high-quality seismic sources with strong repeatability, high stability, cost-effectiveness, and convenience.

In previous studies, various methods have been used for forward modeling and characteristic analysis of seismic wavefields generated by regular trains or HSTs. Fuchs et al. (2018) analyze the seismic vibrations generated by trains and observed that all train signals shared the characteristic feature of sharp, equidistant spectral lines across the entire 2–40 Hz frequency range. Liu and Jiang (2019) propose a frequency-space-time attribute to describe the relation between the HST and seismic wavefield excited by the HST, demonstrating that the generated seismic signals contain diverse geologic environment information. The main methods for simulating seismic waves include the analytical method (Takemiya and Bian, 2005; Wen et al., 2019; Zhang, G. et al., 2019; Yin et al., 2024), finite difference method (FDM) (Wang et al., 2020; Wang et al., 2024a), spectral element method, and finite element method (O'Brien and Rizos, 2005). Frýba (2001) investigates

Manuscript received by the Editor 17 September 2025; revised manuscript received 14 February 2026; published ahead of production 19 April 2026; published online 16 June 2026.
[1]Xi'an Jiaotong University, Xi'an, Shaanxi, China. E-mail: xkwang@xjtu.edu.cn; 3120305117@stu.xjtu.edu.cn; clzx999@stu.xjtu.edu.cn; wencchen@xjtu.edu.cn (corresponding author); 409791715@qq.com; zhouning96@stu.xjtu.edu.cn.
[2]Xi'an University of Technology, Xi'an, Shaanxi, China. E-mail: bluebirdjr@126.com.
[3]China Railway Xi'an Group Co. Ltd, Xi'an, Shaanxi, China. E-mail: 564514829@qq.com.

an elementary theoretical model of a bridge using the integral transformation method. Takemiya and Bian (2007) investigate the vibrations induced by a Shinkansen HST running on a viaduct. They analyzed the characteristics of these vibrations and summarized the key parameters that characterize them. Chen and Cao (2020) regard the HST as a moving linear source and derive Green's function for the seismic data of the HST in an elastic half-space and a full-space model using the principle of superposition. Liu et al. (2021) derive two analytical formulae for the HST-induced seismic wavefield and analyze the wavefield characteristics when the HST runs on a track built on the ground and on viaducts. Wang and Chen (2023) derive a semianalytical formula for the HST wavefield in a two-layered model using the principle of superposition. Wang et al. (2022) investigate the characteristics and factors influencing the synthetic seismic waves generated by an HST passing over a viaduct. They verified that the synthetic seismic records obtained using the Ricker wavelet as the loading function matched well with the actual HST seismic data. Wang et al. (2024b) conduct a full-waveform forward simulation in 3D space of the wavefield excited by an HST running on viaducts using FDM. Lavoué et al. (2021) use the spectral element method to simulate the process of seismic waves generated by a train running on sleepers and analyzed the spectral characteristics of train-generated signals. Gao et al. (2019) apply a 2.5D FDM to investigate the dynamic response of unsaturated ground subjected to moving loads caused by an HST.

Researchers have also explored the application of seismic data from HST sources. Jiang et al. (2022) theoretically analyze the influence of the Doppler effect on the wavefield's spectral features and further verify its influence using observational data from the HST seismic wavefield. They proposed a speed-measurement method based on the Doppler effect and measured the velocity of the medium. Wang et al. (2019) introduce synchrosqueezing time–frequency analysis to HST seismic data. Subsequently, they used a method to accurately characterize the variation in the frequency components of HST seismic signals over time. They further use a single geophone to determine the train state (steady or accelerating) (Wang et al., 2021). Another important application of HST seismic data is subsurface imaging and inversion around railways. Halliday et al. (2008) demonstrate a method to estimate surface-wave interference by measuring suburban seismic surface waves under active and passive conditions. Zhang et al. (2019) propose two methods to reduce source crosstalk in HST seismic interferometric imaging. Liu et al. (2022) use seismic interferometry on HST-induced vibrations and demonstrate that the retrieved surface waves could be used to estimate near-surface velocities. Shao et al. (2022) use distributed acoustic sensing technology to acquire HST seismic data. They obtained subsurface S-wave velocity using seismic interferometry. Mi et al. (2023) stack the stationary-phase segment to reduce the bias generated by trains moving out of the stationary-phase zone of station pairs and use field data to invert the surface waves. Wang et al. (2024) propose a processing scheme to construct broadband virtual shot gathers by distinguishing the moving direction of the HST from the propagation direction of seismic waves and stacking HST events at different speeds. Xia et al. (2025) propose a method for directly extracting the dispersion spectrum from an HST-induced seismic signal through time–frequency decomposition and similarity-based velocity scanning. Based on the study of a theoretical HST seismic source signal, Hu et al. (2019) investigate full-waveform inversion using the acoustic wave equation. Luo et al. (2022) use FDM to simulate a seismic wavefield for an HST running on a viaduct and reconstruct the underground elastic parameters using elastic full-waveform inversion. Shi et al. (2022) propose a method for performing reverse time migration using HST data and use 2D and 3D acoustic wave equations to verify the proposed method. Luo et al. (2023) use HST seismic data to perform elastic reverse time migration to extract subsurface interfaces. Zhou et al. (2024) use the elastic wave equation travel-time inversion method to explore subsurface velocity information using seismic data induced by an HST running on a viaduct.

In summary, researchers have devoted considerable effort to simulating seismic wavefields generated by HST sources and have explored the potential applications of HST seismic data. However, our understanding of HST seismic wavefields is still not comprehensive. As a combined moving source, the HST-induced seismic wavefield exhibits numerous complexities. For example, the directional characteristics of the wavefield interference remain unexplained. The outline of this article is as follows. First, we regard the regularly spaced sleepers as a uniform linear array and simplify the forces exerted by the moving HST as vertically downward concentrated forces acting on the sleepers. Subsequently, by combining the radiation patterns of P- and S-waves excited by a single-point concentrated force with the effect of a uniform array, we derived a theoretical formula for the directional characteristics of the seismic wavefield excited by HST sources. We then used the ABAQUS finite element analysis software to establish a tunnel model for simulation verification. By comparing the theoretical radiation pattern of the HST seismic wavefield with the simulated wavefield, we found strong consistency between the main lobes of the interference patterns. Notably, this conclusion remained valid when we changed the HST speed or the medium parameters.

METHOD

HST subsource function

The HST typically moves along two types of railways: ground tracks and viaducts. In this study, we focused only on the ground-track situation. Before analyzing the mathematical expression of the HST source, it is essential to understand the specific structural parameters of the HST. Figure 1 shows a simplified model of an HST traveling on the ground.

To model the HST source function, we assumed that the HST load was transmitted to the track by a series of wheels moving on the track. Therefore, the moving wheels generate a series of loading functions that interact with the sleepers. It is assumed that each carriage of the train has the same structure and weight and contains four wheelsets. As shown in Figure 1, each carriage contains two bogies, and each bogie has two wheelsets. The length of each carriage is determined using L. d_1 represents the distance between two wheelsets within one bogie, d_2 represents the distance between two bogies within one carriage, and $d_3 = d_1 + d_2$. d_0 is the distance between the first wheelset of the HST and point A, as shown in Figure 1. To ensure that the time at which the first pair of wheels passes point A is zero and to maintain consistency in the subsequent formulas, we set d_0 to 0. d_s is the distance between adjacent sleepers. To simplify the analysis, in the first step, we assumed that the loading function of each wheelset was a Dirac delta function. Setting the moment when the first wheelset passes point A (Figure 1) as $t = 0$, the HST subsource function (source function for a single sleeper or pier) at point A can be expressed as

$$p(t) = \sum_{m=0}^{N_t-1}\sum_{k=0}^{3}\delta\left(t - \frac{d_k}{v_t} - \frac{mL}{v_t}\right), \tag{1}$$

where N_t is the number of train carriages and v_t is the moving speed of the HST. We observe that equation 1 represents the summation of impulse functions with different time delays. Using the properties of the impulse function and convolution, equation 1 can be formulated as follows (Wang et al., 2024):

$$p(t) = c(t) * h(t) = c(t) * \sum_{m=0}^{N_t-1}\delta\left(t - \frac{mL}{v_t}\right), \tag{2}$$

where $*$ represents the convolution operation, and $h(t)$ represents the periodic input of N_t carriages, which is

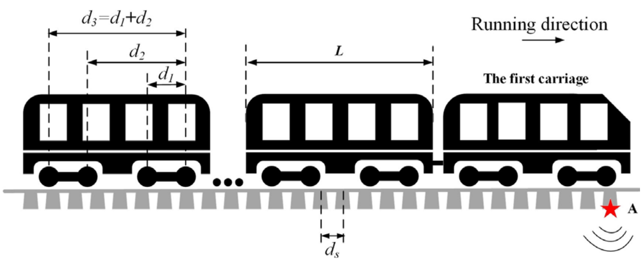

Figure 1. Sketch of the high-speed trains traveling on the ground.

$$h(t) = \sum_{m=0}^{N_t-1}\delta\left(t - m\frac{L}{v_t}\right), \tag{3}$$

and $c(t)$ represents the loading function for a single carriage, which can be further formulated as

$$\begin{aligned} c(t) &= \delta\left(t - \frac{d_0}{v_t}\right) + \delta\left(t - \frac{d_1}{v_t}\right) + \delta\left(t - \frac{d_2}{v_t}\right) + \delta\left(t - \frac{d_3}{v_t}\right) \\ &= \delta(t) + \delta\left(t - \frac{d_1}{v_t}\right) + \delta\left(t - \frac{d_2}{v_t}\right) + \delta\left(t - \frac{d_1 + d_2}{v_t}\right) \\ &= c_1(t) * c_2(t) \end{aligned}, \tag{4}$$

with

$$\begin{cases} c_1(t) = \delta(t) + \delta\left(t - \dfrac{d_1}{v_t}\right) \\ c_2(t) = \delta(t) + \delta\left(t - \dfrac{d_2}{v_t}\right) \end{cases}. \tag{5}$$

Performing the Fourier transform on equations 3 and 5 gives

$$H(f) = \frac{\sin\left(\pi f \frac{N_t L}{v_t}\right)}{\sin\left(\pi f \frac{L}{v_t}\right)}\exp\left(-j\pi f\frac{(N_t - 1)L}{v_t}\right), \tag{6}$$

$$\begin{cases} C_1(f) = 2\cos\left(\pi f\dfrac{d_1}{v_t}\right)\exp\left(-j\pi f\dfrac{d_1}{v_t}\right) \\ C_2(f) = 2\cos\left(\pi f\dfrac{d_2}{v_t}\right)\exp\left(-j\pi f\dfrac{d_2}{v_t}\right) \end{cases}, \tag{7}$$

where f is the frequency and j is the imaginary unit. Therefore, the amplitude spectrum of the HST subsource function at point A is

$$\begin{aligned} |P(f)| &= |C_1(f)||C_2(f)||H(f)| \\ &= 4\left|\cos\left(\pi f\frac{d_1}{v_t}\right)\right|\left|\cos\left(\pi f\frac{d_2}{v_t}\right)\right|\left|\frac{\sin\left(\pi f\frac{N_t L}{v_t}\right)}{\sin\left(\pi f\frac{L}{v_t}\right)}\right| \end{aligned}. \tag{8}$$

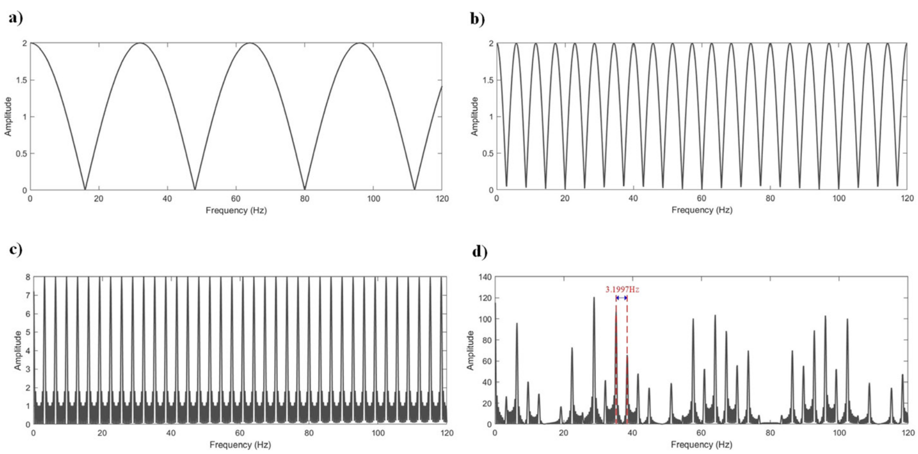

Figure 2. Amplitude spectra. (a) $|C_1(f)|$, (b) $|C_2(f)|$, (c) $|H(f)|$, and (d) $|P(f)|$.

Referring to a typical HST (CRH380) in China, the carriage length is 25 m, and the wheelset distance d_1 and bogie distance d_2 are 2.5 and 14.5 m, respectively. The HST usually consists of eight carriages. We set the HST speed v_t = 80 m/s. The corresponding amplitude spectra $|C_1(f)|$, $|C_2(f)|$, $|H(f)|$, and $|P(f)|$ can then be obtained, as shown in Figure 2a–2d.

Equation 8 shows that the periodic signal $|H(f)|$ in the frequency domain is multiplied by the envelope $|C_1(f)|\,|C_2(f)|$. Therefore, the amplitude spectrum of $|P(f)|$ retains many of the key characteristics of $|H(f)|$. As shown in Figure 2c and 2d, the behaviors of $|P(f)|$ exhibit narrow discrete spectral lines, which originate from its periodic structure $|H(f)|$. Additionally, the peak frequencies and intervals between spectral peaks are nearly identical in both spectra. We selected two adjacent peak spectral lines in Figure 2d, and the frequency interval between them was 3.1997 Hz, which is consistent with that derived from the train speed υ_t and carriage length L (Wang et al., 2024; $\Delta f = \upsilon_t \div L = 80\ \mathrm{m/s} \div 25\ \mathrm{m} = 3.2\ \mathrm{Hz}$, where Δf is the frequency interval).

In the previous analysis, the Dirac delta function was used for mathematical modeling. However, because the rail is an elastic beam in practical scenarios, we adopted the Ricker wavelet as the loading function. The Ricker wavelet is

$$r(t) = \left[1 - 2(\pi f_0 t)^2\right] e^{-(\pi f_0 t)^2}, \tag{9}$$

where f_0 denotes the dominant frequency. The amplitude spectrum of the Ricker wavelet (Wang, 2015) can be expressed as

$$R(f) = \frac{2f^2}{\sqrt{\pi} f_0^3} \exp\left(-\frac{f^2}{f_0^2}\right). \tag{10}$$

After introducing the Ricker wavelet, the HST subsource function at point A can be expressed as follows:

$$s(t) = p(t) * r(t) = \sum_{m=0}^{N_t-1} \sum_{k=0}^{3} r\left(t - \frac{d_k}{\upsilon_t} - \frac{mL}{\upsilon_t}\right). \tag{11}$$

The amplitude spectrum of the HST subsource function at point A can be expressed as follows:

$$|S(f)| = 4\left|\cos\left(\pi f \frac{d_1}{\upsilon_t}\right)\right| \left|\cos\left(\pi f \frac{d_2}{\upsilon_t}\right)\right| \left|\frac{\sin\left(\pi f \frac{N_t L}{\upsilon_t}\right)}{\sin\left(\pi f \frac{L}{\upsilon_t}\right)}\right| |R(f)|. \tag{12}$$

The dominant frequency of the Ricker wavelet was set to 15 Hz. The time-domain waveform and normalized Fourier amplitude spectrum of the HST subsource are shown in Figures 3 and 4, respectively. After introducing the Ricker wavelet, the amplitude spectrum of the HST subsource function (Figure 4) still exhibited the characteristic feature of a typical equal-peak-interval narrowband spectrum. The interval between two adjacent spectral lines in Figure 4 was 3.1996 Hz, which is very close to 3.2 Hz. $|P(f)|$ exhibits typical equidistant narrowband discrete spectral characteristics (as shown in Figure 2d), whereas $|R(f)|$ demonstrates broadband continuous spectral features. Therefore, the spectrum peak interval of $|S(f)|$ (as shown in Figure 4) is dominated by $|P(f)|$, whereas the spectrum peak amplitude is affected by $|R(f)|$, which restricts these spectral peaks within 45 Hz.

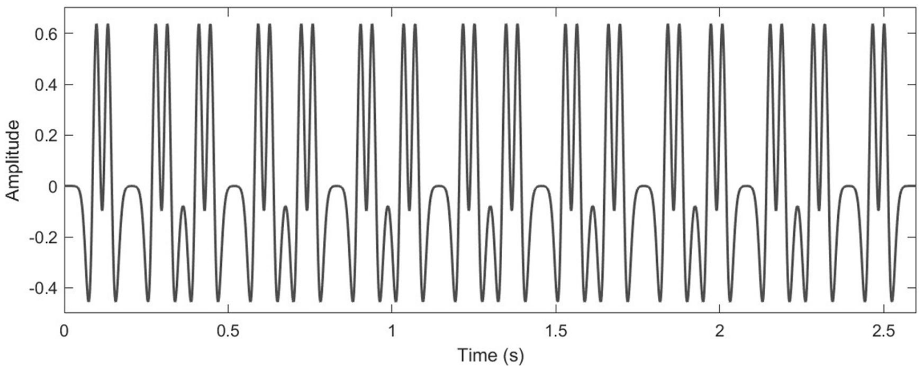

Figure 3. Time-domain waveform of the high-speed train subsource.

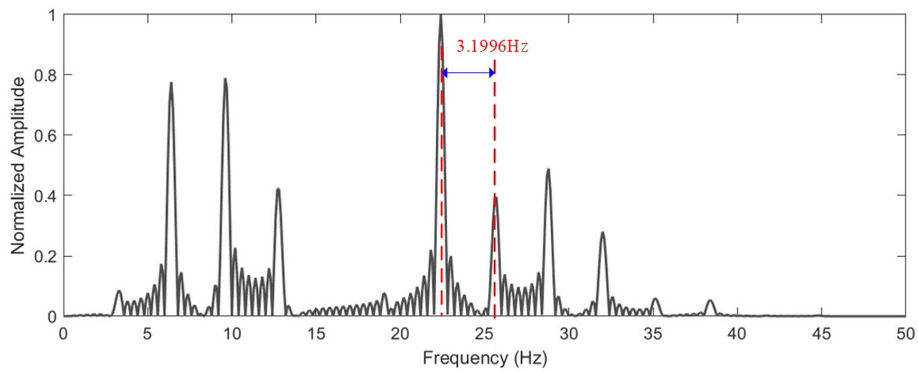

Figure 4. Normalized Fourier amplitude spectrum of the high-speed train subsource.

Point source with concentrated force

The radiation pattern of a seismic wavefield excited by a single-point concentrated force affects its directional characteristics. In an infinitely homogeneous elastic medium, the displacement field induced by a concentrated force primarily comprises P- and S-waves. The S-wave is polarized in a plane defined by the propagation direction of the wave and direction of the applied force (Xu and Zhou, 1982). Based on source theory (Chen and Gu, 2023), the radiation pattern factors for P- and S-waves generated by a concentrated force source can be expressed as

$$\begin{cases} A_{\mathrm{P}}(\theta) = \cos\theta \\ A_{\mathrm{S}}(\theta) = -\sin\theta\text{'} \end{cases} \tag{13}$$

where θ is the angle between the direction of wave propagation and direction of the concentrated force, $A_{\mathrm{P}}(\theta)$ is the radiation pattern factor for P-waves, and $A_{\mathrm{S}}(\theta)$ is the radiation pattern factor for S-waves. In this study, the direction of the concentrated force was vertically downward because the HST–rail interaction force was strongest in this direction. The radiation patterns

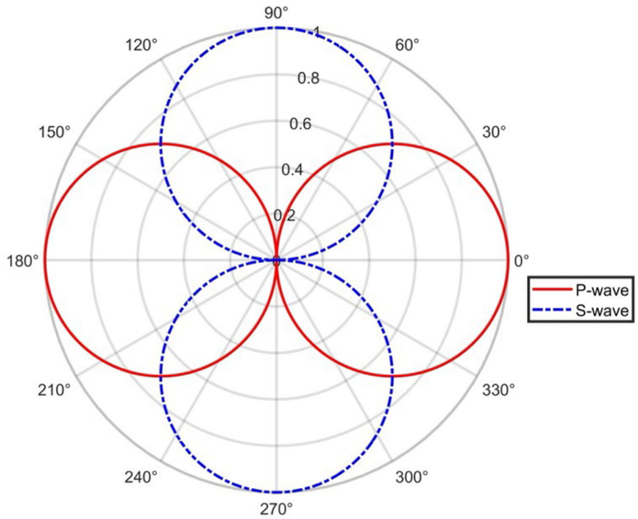

Figure 5. Radiation patterns of P- and S-waves generated by a single concentrated force.

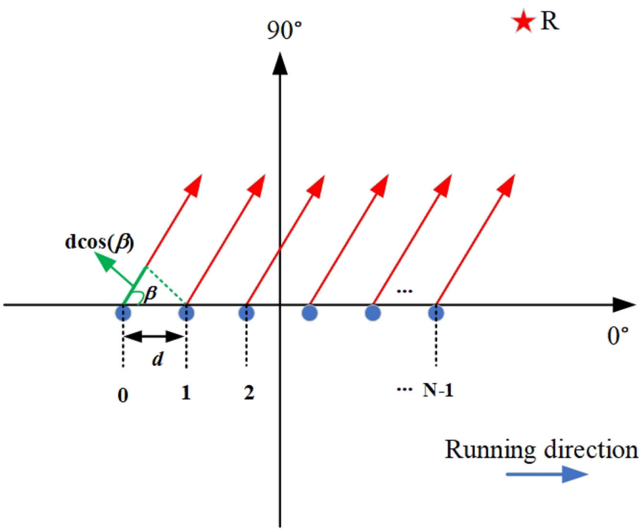

Figure 6. Schematic diagram of a uniform linear array.

of P- and S-waves generated by a single concentrated force are shown in Figure 5.

HST source based on uniform linear array theory

Sleepers serve as structural members that link the rails to the ground, transmitting dynamic forces from the train to the subgrade. Given their regular spacing in the HSR, the sleeper arrangement can be conceptualized as a linear array, with each sleeper acting as a basic element. In this section, a uniform linear array is used to represent a series of uniformly spaced sleepers. Based on linear array theory, we derived an array factor expression for the seismic wavefield generated by an HST source. We then analyzed the amplitude of the array factor under different conditions. First, we plotted a schematic of the uniform linear array, as shown in Figure 6.

The blue dots in Figure 6 represent uniformly distributed array elements (sleepers), the red line indicates the wave propagation direction, the blue arrow indicates the running direction of the HST, and R is the far-field receiving point. We assumed that the seismic waves excited by the sleepers propagated through the medium without amplitude attenuation. However, seismic waves excited from sleepers at different locations exhibit differences in time delay and propagation distance. Therefore, the seismic waves received at point R from the array can be expressed as

$$\begin{aligned}
\mathrm{s}_0(t) &= s\left(t-\frac{D}{v_m}\right) \\
\mathrm{s}_1(t) &= s\left(t-\frac{d}{v_t}-\frac{D-\mathrm{d}\cos(\beta)}{v_m}\right) \\
\mathrm{s}_2(t) &= s\left(t-\frac{2d}{v_t}-\frac{D-2\mathrm{d}\cos(\beta)}{v_m}\right) \\
&\vdots \\
\mathrm{s}_{N-1}(t) &= s\left(t-\frac{(N-1)d}{v_t}-\frac{D-(N-1)\mathrm{d}\cos(\beta)}{v_m}\right)
\end{aligned}, \quad (14)$$

where v_m is the wave velocity, D is the wave propagation distance from the position of the 0th element to point R, d is the spacing between adjacent array elements (sleeper interval), N is the number of array elements, and β is the angle between the wave propagation direction toward point R and the running direction of the HST. By performing the Fourier transform on equation 14, we obtain

$$\begin{aligned}
&\mathrm{S}_0(f)=\mathrm{S}(f)e^{-j2\pi f\frac{D}{v_m}} \\
&\mathrm{S}_1(f)=\mathrm{S}(f)e^{-j2\pi f\frac{D}{v_m}}e^{j2\pi f\left(\frac{\mathrm{d}\cos(\beta)}{v_m}-\frac{d}{v_t}\right)} \\
&\mathrm{S}_2(f)=\mathrm{S}(f)e^{-j2\pi f\frac{D}{v_m}}e^{j2\pi f\left(2\left(\frac{\mathrm{d}\cos(\beta)}{v_m}-\frac{d}{v_t}\right)\right)} \\
&\vdots \\
&\mathrm{S}_{N-1}(f)=\mathrm{S}(f)e^{-j2\pi f\frac{D}{v_m}}e^{j2\pi f\left((N-1)\left(\frac{\mathrm{d}\cos(\beta)}{v_m}-\frac{d}{v_t}\right)\right)}
\end{aligned}. \quad (15)$$

Using the principle of superposition, the total seismic waves received at point R are

$$\begin{aligned}
Y(f) &= \sum_{n=0}^{N-1}\mathrm{S}(f)e^{-j2\pi f\frac{D}{v_m}}e^{j2\pi fn\left(\frac{\mathrm{d}\cos(\beta)}{v_m}-\frac{d}{v_t}\right)} \\
&= \mathrm{S}(f)e^{-j2\pi f\frac{D}{v_m}}\sum_{n=0}^{N-1}e^{j2\pi fn\left(\frac{\mathrm{d}\cos(\beta)}{v_m}-\frac{d}{v_t}\right)} \\
&= \mathrm{S}(f)e^{-j2\pi f\frac{D}{v_m}}\frac{1-e^{j2\pi f\left(\frac{\mathrm{d}\cos(\beta)}{v_m}-\frac{d}{v_t}\right)N}}{1-e^{j2\pi f\left(\frac{\mathrm{d}\cos(\beta)}{v_m}-\frac{d}{v_t}\right)}}
\end{aligned}. \quad (16)$$

Calculating the magnitude of equation 16, we obtain

$$\begin{aligned}
|Y(f)| &= \left|\sum_{n=0}^{N-1}\mathrm{S}(f)e^{-j2\pi f\frac{D}{v_m}}e^{j2\pi fn\left(\frac{\mathrm{d}\cos(\beta)}{v_m}-\frac{d}{v_t}\right)}\right| \\
&= |\mathrm{S}(f)|\left|\frac{1-e^{j2\pi f\left(\frac{\mathrm{d}\cos(\beta)}{v_m}-\frac{d}{v_t}\right)N}}{1-e^{j2\pi f\left(\frac{\mathrm{d}\cos(\beta)}{v_m}-\frac{d}{v_t}\right)}}\right| \\
&= |\mathrm{S}(f)|\left|\frac{\sin\left(\pi fdN\left(\frac{\cos(\beta)}{v_m}-\frac{1}{v_t}\right)\right)}{\sin\left(\pi fd\left(\frac{\cos(\beta)}{v_m}-\frac{1}{v_t}\right)\right)}\right|
\end{aligned}. \quad (17)$$

Thus, the array factor can be obtained from equation 17 as follows:

$$|A_F(f,d,\beta,v_m,v_t,N)| = \left|\frac{\sin\left(\pi f d N\left(\frac{\cos(\beta)}{v_m}-\frac{1}{v_t}\right)\right)}{\sin\left(\pi f d\left(\frac{\cos(\beta)}{v_m}-\frac{1}{v_t}\right)\right)}\right|. \tag{18}$$

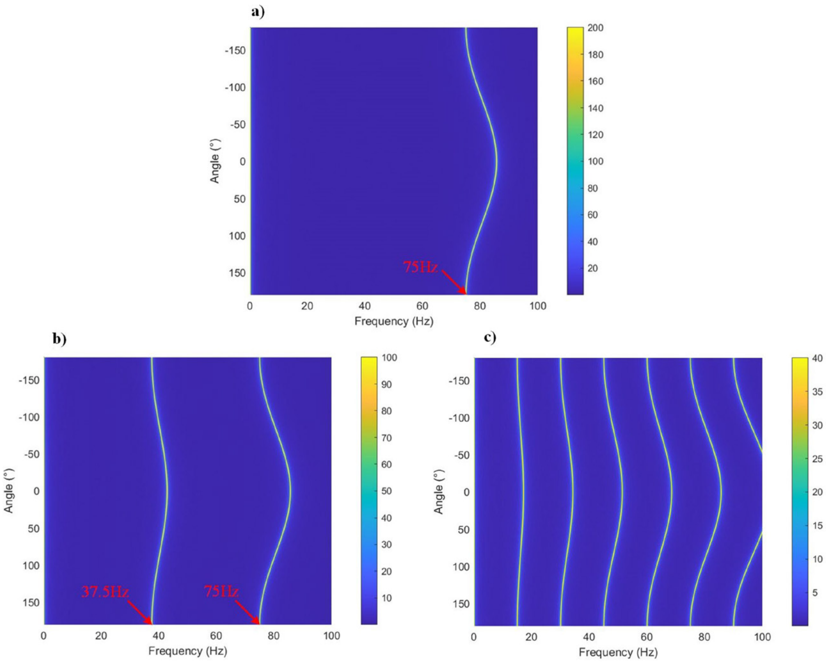

Figure 7. Magnitude of the array factor for $v_t = 80$ m/s. (a) Array element spacing $d = 1$ m, (b) array element spacing $d = 2$ m, and (c) array element spacing $d = 5$ m.

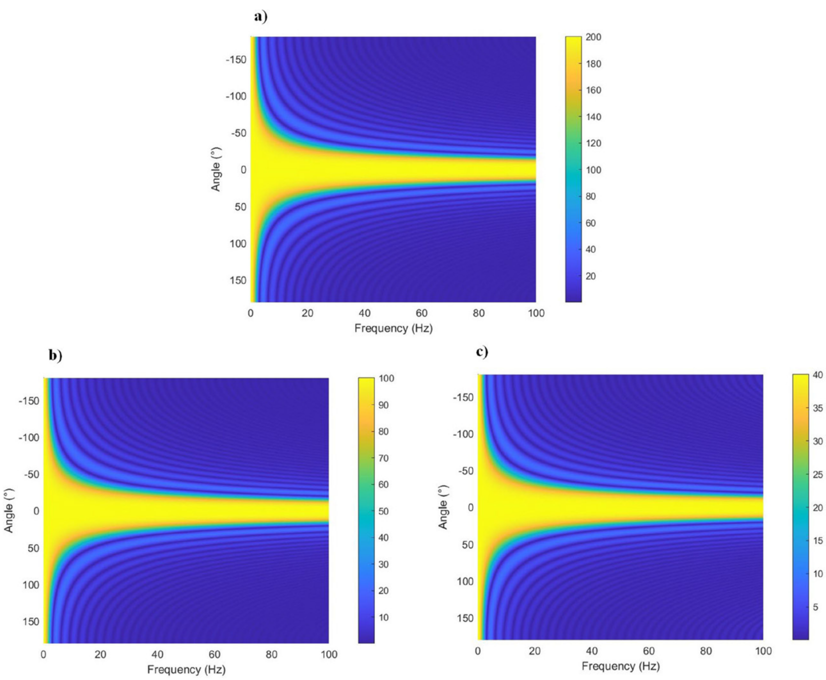

Figure 8. Magnitude of the array factor for $v_t = v_m$. (a) Array element spacing $d = 1$ m, (b) array element spacing $d = 2$ m, and (c) array element spacing $d = 5$ m.

By carefully examining equation 18, we observe that the magnitude of the array factor $A_F(f,d,\beta,v_m,v_t,N)$ is determined by multiple parameters. Next, we analyzed in detail how the magnitude of the array factor varies with different parameter values. First, we define $L_t = dN$, where L_t represents the total HST length. When the HST is traveling on the ground, the entire linear array can also be considered moving. Next, we provide relevant examples.

For the case of $v_m = 1206$ m/s (this wave velocity will be used in subsequent sections) and the HST speed $v_t = 80$ m/s, the variation in the magnitude of the array factor is shown in Figure 7. The horizontal axis represents the frequency range from 0 to 100 Hz, and the vertical axis corresponds to the angle β. As shown in Figure 7a, there is only one bright curve. This indicates that when the element spacing is small ($d = 1$ m) and the frequency is below 75 Hz, the magnitude of the array factor is very small for any value of angle β. Furthermore, we can conclude that when the element spacing is small ($d = 1$ m) and the frequency is below 75 Hz, the wavefield excited by the HST source shows no significant interference phenomenon in the entire plane. Moreover, we observe that as the element spacing increases, the number of bright curves in the figure also increases. This implies that with larger element spacing, the wavefield excited by the HST source is more likely to exhibit multifrequency interference phenomena in the plane.

For the case of $v_m = 1206$ m/s and HST speed $v_t = v_m$, the variation in the magnitude of the array factor is shown in Figure 8. From the analysis of equation 18, it can be seen that when β approaches zero, the numerator and denominator of the array factor approach zero. Using the rule of taking the limit, the array factor approaches N. This result indicates that regardless of the frequency value, the seismic waves form a strong wavefield in the running direction.

For the extreme case of $v_m = 1206\ \mathrm{m/s}$ and HST speed $v_t = 10v_m$, the variation in the magnitude of the array factor is shown in Figure 9. From the analysis of equation 18, it can be observed that the value of v_t is large and $1/v_t$ approaches zero. When β approaches $\pm 90^\circ$, the numerator and denominator of the array factor approach zero. Using the rule of taking the limit, the array factor approaches N. This result indicates that seismic waves form strong waves in the direction perpendicular to the running direction.

In the previous section, several examples were presented to demonstrate the array factor characteristics. Next, by using the radiation pattern factors for P- and S-waves excited by a single-point force source, as shown in equation 13, we can derive the radiation pattern factors for P- and S-waves excited by the HST source:

$$\begin{cases} |A_{\mathrm{P\_train}}| = |A_{\mathrm{P}}(\theta) \cdot A_F(f, d, \beta, v_p, v_t, N)| \\ \quad = \left| \cos\theta \cdot \dfrac{\sin\left(\pi f d N\left(\frac{\cos(\beta)}{v_p} - \frac{1}{v_t}\right)\right)}{\sin\left(\pi f d\left(\frac{\cos(\beta)}{v_p} - \frac{1}{v_t}\right)\right)} \right| \\ |A_{\mathrm{S\_train}}| = |A_{\mathrm{S}}(\theta) \cdot A_F(f, d, \beta, v_s, v_t, N)| \\ \quad = \left| \sin\theta \cdot \dfrac{\sin\left(\pi f d N\left(\frac{\cos(\beta)}{v_s} - \frac{1}{v_t}\right)\right)}{\sin\left(\pi f d\left(\frac{\cos(\beta)}{v_s} - \frac{1}{v_t}\right)\right)} \right| \end{cases}, \tag{19}$$

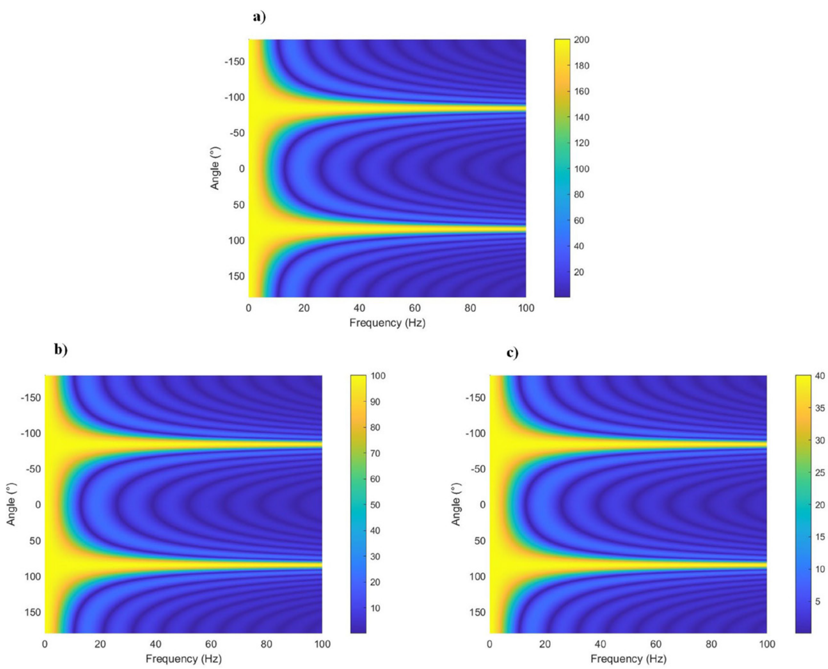

Figure 9. Magnitude of the array factor for $v_t = 10v_m$. (a) Array element spacing $d = 1$ m, (b) array element spacing $d = 2$ m, and (c) array element spacing $d = 5$ m.

where $|A_{\mathrm{P\_train}}|$ and $|A_{\mathrm{S\_train}}|$ are the radiation pattern factors for P- and S-waves excited by the HST source, respectively. By considering equation 19 as the system response and the input source function (equation 12), we can derive the expression for the output wavefield excited by the HST source:

$$\begin{cases} |Y_{\mathrm{P\_train}}| = |S(f)||A_{\mathrm{P_{train}}}| \\ = |S(f)| \left| \cos\theta \cdot \dfrac{\sin\left(\pi f d N\left(\frac{\cos(\beta)}{v_p} - \frac{1}{v_t}\right)\right)}{\sin\left(\pi f d\left(\frac{\cos(\beta)}{v_p} - \frac{1}{v_t}\right)\right)} \right| \\ |Y_{\mathrm{S\_train}}| = |S(f)||A_{\mathrm{S_{train}}}| \\ = |S(f)| \left| \sin\theta \cdot \dfrac{\sin\left(\pi f d N\left(\frac{\cos(\beta)}{v_s} - \frac{1}{v_t}\right)\right)}{\sin\left(\pi f d\left(\frac{\cos(\beta)}{v_s} - \frac{1}{v_t}\right)\right)} \right| \end{cases}. \tag{20}$$

To facilitate understanding, we illustrate the angles θ and β in Figure 10. The horizontal gray and vertical yellow planes represent the z-axis and y-axis sections, respectively. The blue dot represents an element of the uniform linear array, the blue arrow represents the wave propagation direction within the z-axis section, and the red arrow represents the wave propagation direction along the x-axis.

NUMERICAL EXAMPLES

In this section, the finite element analysis software ABAQUS is used to establish a seismic wavefield model for an HST source in a tunnel environment. We chose the tunnel-mode scenario because it allows the medium to be modeled as a simple infinite space. Because absorbing boundary conditions are used, the excited seismic wavefield is predominantly composed of body waves, which facilitates comparison between the theoretical analysis and the simulation results. Based on the simulation results, the characteristics of the seismic wavefield generated by the HST were analyzed. Furthermore, we compared the simulated data with the theoretical radiation patterns to verify the theoretical formula.

HST seismic data simulation with a finite element model

We simplified the mountain as a rectangular prism and the tunnel as a hollow cylindrical structure. The

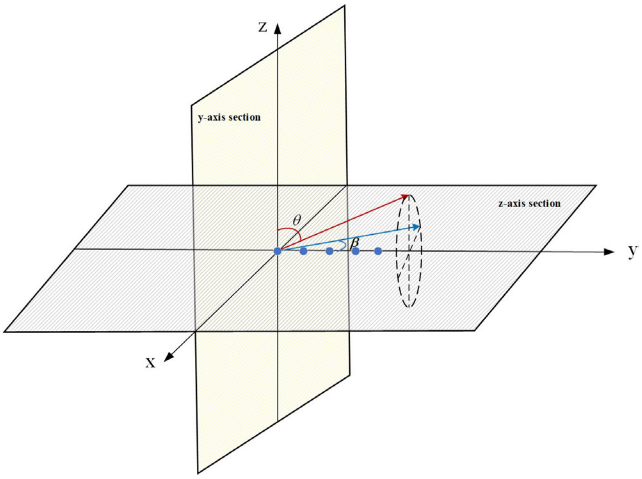

Figure 10. Schematic diagram of the angles θ and β.

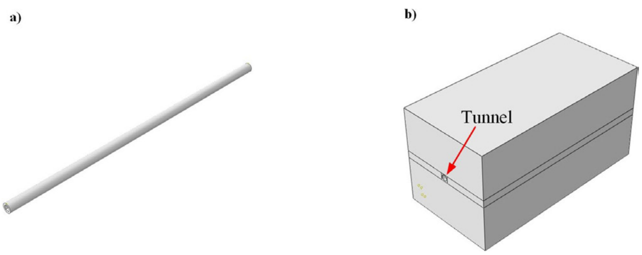

Figure 11. Model component diagrams. (a) Tunnel and (b) mountain.

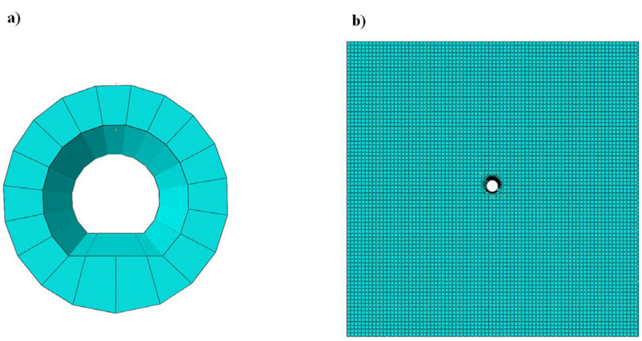

Figure 12. Component mesh front view. (a) Tunnel and (b) mountain.

parameters for the mountain model are as follows: dimensions of 800 m × 600 m × 400 m (length × width × height), density of 2000 kg/m³, Young's modulus of 7.09 × 10^9 Pa, and Poisson's ratio of 0.2188 ($v_p = 2010\,\mathrm{m/s}$ and $v_s = 1206\,\mathrm{m/s}$ in this medium). For the tunnel model, the parameters are dimensions of 800 m × 14 m × 14 m, density of 2500 kg/m³, Young's modulus of 3.25 × 10^{10} Pa, and Poisson's ratio of 0.2 ($v_p = 3800\,\mathrm{m/s}$ and $v_s = 2327\,\mathrm{m/s}$

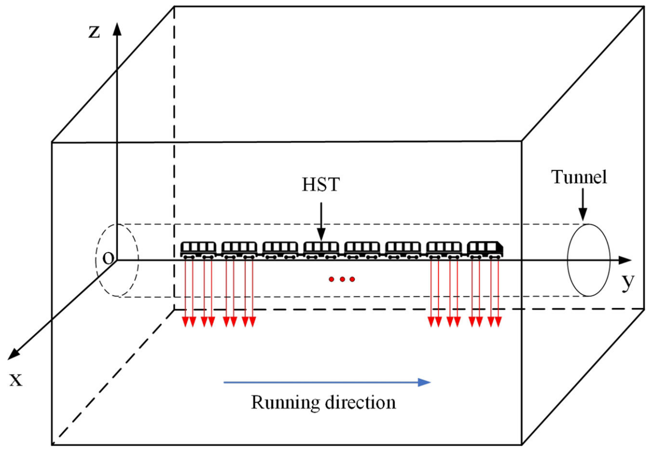

Figure 13. Schematic diagram of source loading in the model.

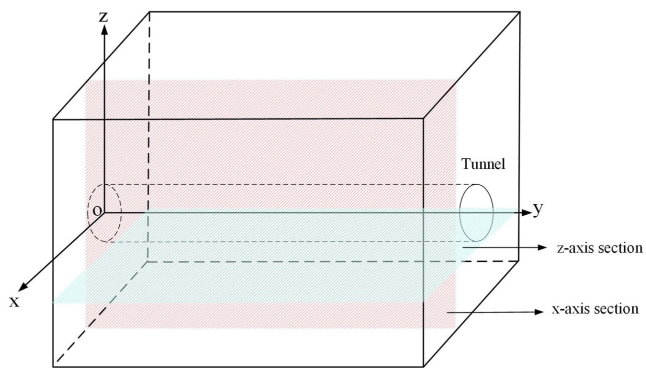

Figure 14. Schematic diagram of the x-axis and z-axis sections.

in this medium). The contact interface between the tunnel and mountain was constrained using tie binding, with the inner surface of the tunnel set as a free surface. To reduce wave reflections, the front and rear surfaces of the tunnel, along with the six mountain surfaces, were assigned infinite-element absorbing boundaries with a thickness of 100 m. The component diagrams of the tunnel and mountain models, as well as the mesh division diagrams, are shown in Figures 11 and 12.

Referring to a typical HST (CRH380) in China, the number of train carriages was set to eight. We adopted a Ricker wavelet with a dominant frequency of 15 Hz as the loading function. The load points were spaced 2 m apart with a vertical downward concentrated force of 70 kN. A schematic of the source loading is shown in Figure 13.

We present the simulation results using wavefield snapshots of different cross-sections. Because we focused on the wavefield generated by the array, we illustrate only the x-axis and z-axis sections, as shown in Figure 14.

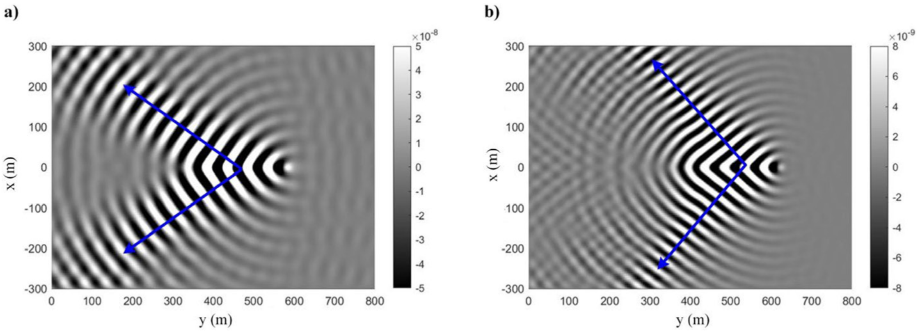

Figure 15. Snapshot of the wavefield at the section $z = -15$ m. The blue arrow indicates the main lobe direction of the seismic waves. (a) $v_t = 60$ m/s and (b) $v_t = 80$ m/s.

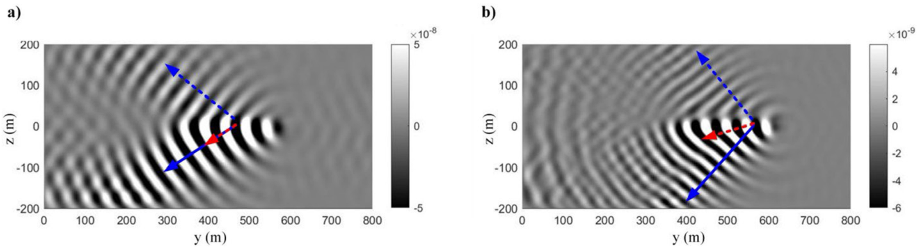

Figure 16. Snapshot of the wavefield at the section $x = 20$ m. The blue and red arrows indicate the main lobe directions of the waves. (a) $v_t = 60$ m/s and (b) $v_t = 80$ m/s.

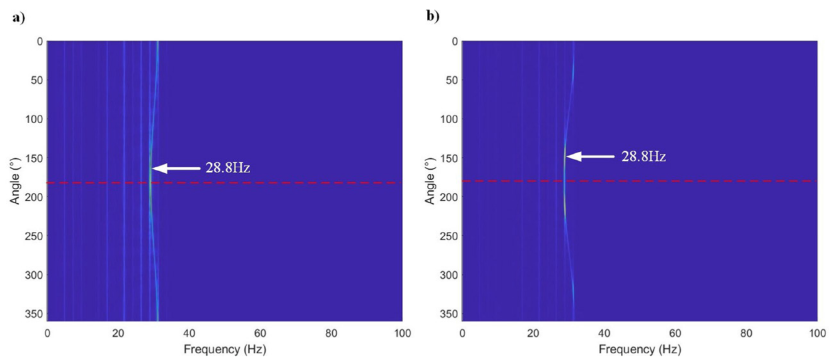

Figure 17. Diagrams of the theoretical strongest frequency corresponding to wavefield interference for $v_t = 60$ m/s. (a) $v_m = 2010$ m/s and (b) $v_m = 1206$ m/s.

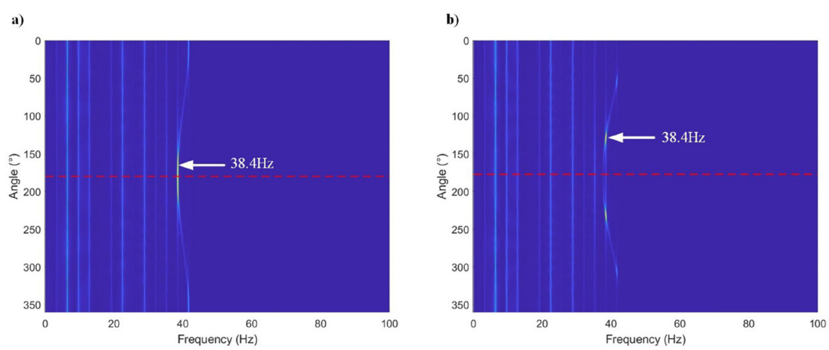

Figure 18. Diagrams of the theoretical strongest frequency corresponding to wavefield interference for $v_t = 80$ m/s. (a) $v_m = 2010$ m/s and (b) $v_m = 1206$ m/s.

The simulated wavefield snapshots in the z-axis and x-axis sections are shown in Figures 15 and 16, respectively. The HST speeds were set to 60 and 80 m/s. Stable and distinct wavefield interference phenomena can be observed in Figures 15 and 16. As the train speed increases from 60 to 80 m/s, the main lobe angle of the wavefield interference changes, as indicated by the arrows in Figures 15 and 16. From Figure 16, we observe that the seismic wave intensity on the negative half-axis of the z-axis is greater than that on the positive half-axis, owing to the concentrated force applied in the negative z-axis direction. Furthermore, when the train speed changed from 60 to 80 m/s, the main lobes also showed a tendency to separate, as indicated by the blue and red arrows in Figure 16.

Comparison of the theoretical radiation pattern and simulated wavefield snapshot

In this section, we present a comparative analysis of the theoretical radiation patterns and simulated wavefield snapshots. First, we plotted the theoretical radiation patterns based on the previously derived formulas. We set the parameters to $d_1 = 2.5$ m, $d_2 = 14.5$ m, $L = 25$ m, $d = 2$ m, and $N = 100$. Subsequently, based on equations 12 and 17, we plotted the diagrams of the theoretical strongest frequency corresponding to the wavefield interference for $v_t = 60$ m/s and $v_t = 80$ m/s, as shown in Figures 17 and 18, respectively.

From Figures 17 and 18, we observe that when the speed $v_t = 60$ m/s and $v_t = 80$ m/s, the theoretical strongest frequencies corresponding to wavefield interference are 28.8 and 38.4 Hz, respectively. Next, based on equations 12 and 20, we plotted the theoretical radiation pattern figures

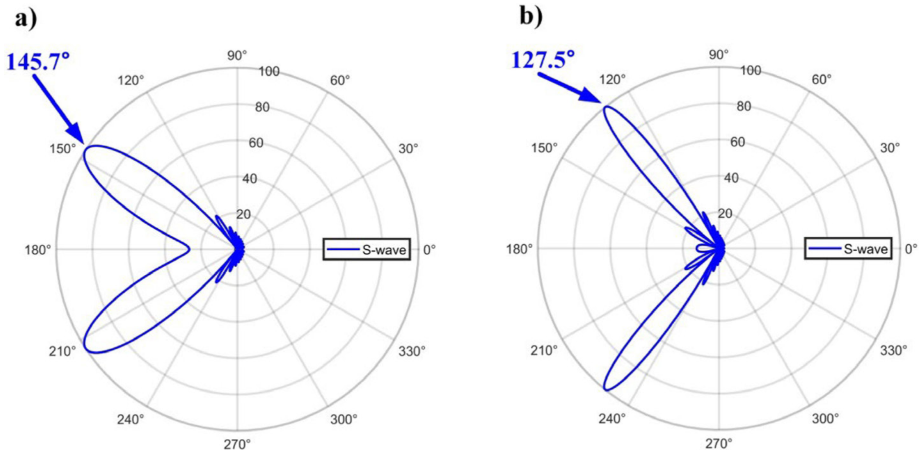

Figure 19. Theoretical radiation patterns at the z-axis section. $d_1 = 2.5$ m, $d_2 = 14.5$ m, $L = 25$ m, $N_t = 8$, $d = 2$ m, $N = 100$, and $\upsilon_s = 1206$ m/s. (a) $\upsilon_t = 60$ m/s, $f = 28.8$ Hz; (b) $\upsilon_t = 80$ m/s, $f = 38.4$ Hz.

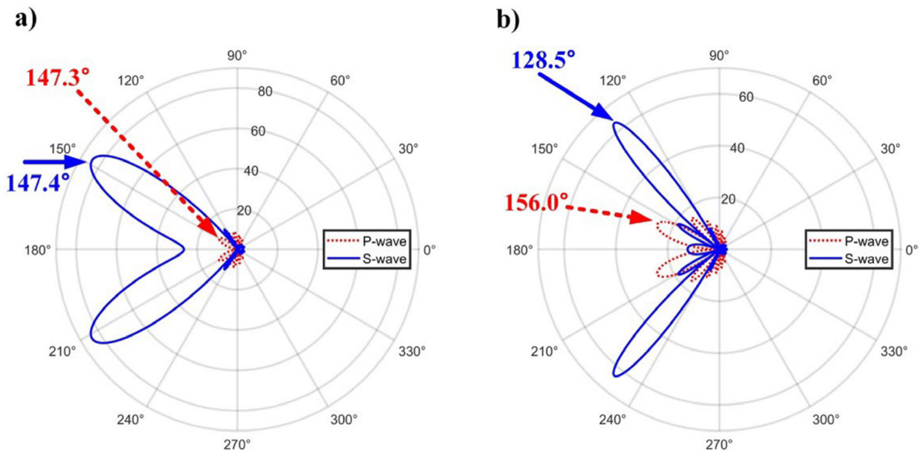

Figure 20. Theoretical radiation patterns at the x-axis section. $d_1 = 2.5$ m, $d_2 = 14.5$ m, $L = 25$ m, $N_t = 8$, $d = 2$ m, $N = 100$, $\upsilon_p = 2010$ m/s, and $\upsilon_s = 1206$ m/s. (a) $\upsilon_t = 60$ m/s, $f = 28.8$ Hz and (b) $\upsilon_t = 80$ m/s, $f = 38.4$ Hz.

in polar coordinates for different HST speeds. A brief explanation is necessary. In equation 19, for the z-axis section, with $\theta = \pi/2$, the result is $A_P(\theta) = 0$ and $A_S(\theta) = 1$. Therefore, theoretically, only S-waves are present in the z-axis section, with no P-waves. For the x-axis section, there is $\theta \in (0, \pi)$. Therefore, theoretically, P- and S-waves are present in the x-axis section. The theoretical radiation pattern figures for the z-axis and x-axis sections are shown in Figures 19 and 20, respectively.

To compare the results more clearly, we combined the theoretical radiation pattern figures with the simulated wavefield snapshots. The combined figures are shown in Figures 21 and 22. In Figures 21 and 22, the theoretical radiation patterns show strong consistency with the directions and angles of the main interference lobes in the wavefield snapshots. When the HST speed increased from 60 to 80 m/s, separation of the main interference lobes was observed in the x-axis section. The results of the comparative analysis validate the reliability of the proposed theoretical formula.

We also conducted a comparative analysis after changing the density of the medium. A careful reader will notice that changing the medium density is equivalent to changing the wave velocity in equation 21:

$$\begin{cases} \upsilon_p = \sqrt{\dfrac{E(1-\sigma)}{\rho(1+\sigma)(1-2\sigma)}} \\ \upsilon_s = \sqrt{\dfrac{E}{2\rho(1+\sigma)}}, \end{cases} \tag{21}$$

where E is Young's modulus, σ is Poisson's ratio, and ρ is the medium density. For convenience, we kept Young's modulus and Poisson's ratio constant and varied only the medium density. At an HST speed of 80 m/s, when the medium density was changed from 2000 to 1300 kg/m³, the P-wave velocity increased from 2010 to 2493 m/s, and the S-wave velocity increased from 1206 to 1496 m/s. The theoretical radiation patterns obtained after reducing the medium density are shown in Figure 23. The combined images are shown in Figure 24a and 24b.

In Figure 24a and 24b, after reducing the medium density of the model, we observe that the main lobe angle of the wavefield interference changes, and the theoretical radiation pattern still shows strong consistency with the directions and angles of the main interference lobes in the wavefield snapshots.

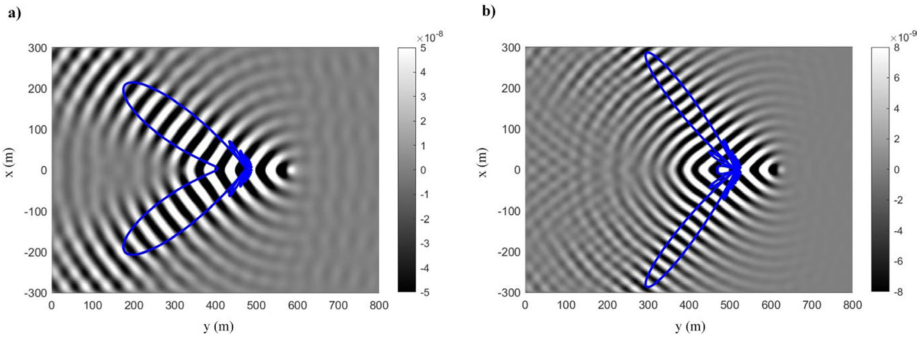

Figure 21. Combined figure of the theoretical radiation patterns (blue lines are the theoretical radiation patterns of S-waves) and simulated wavefield snapshots at the z-axis section. (a) $v_t = 60$ m/s and (b) $v_t = 80$ m/s.

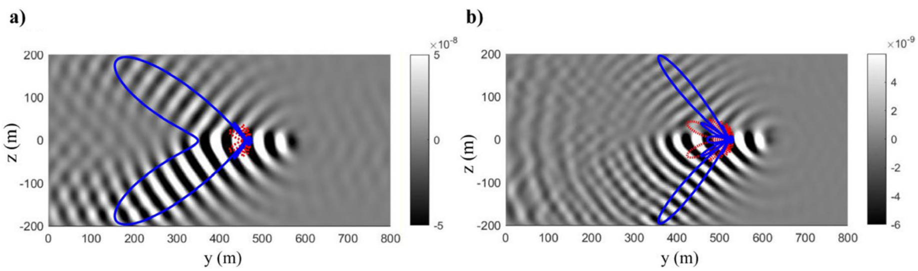

Figure 22. Combined figure of the theoretical radiation patterns (red lines are the theoretical radiation patterns of P-waves, and blue lines are the theoretical radiation patterns of S-waves) and simulated wavefield snapshots at the x-axis section. (a) $v_t = 60$ m/s and (b) $v_t = 80$ m/s.

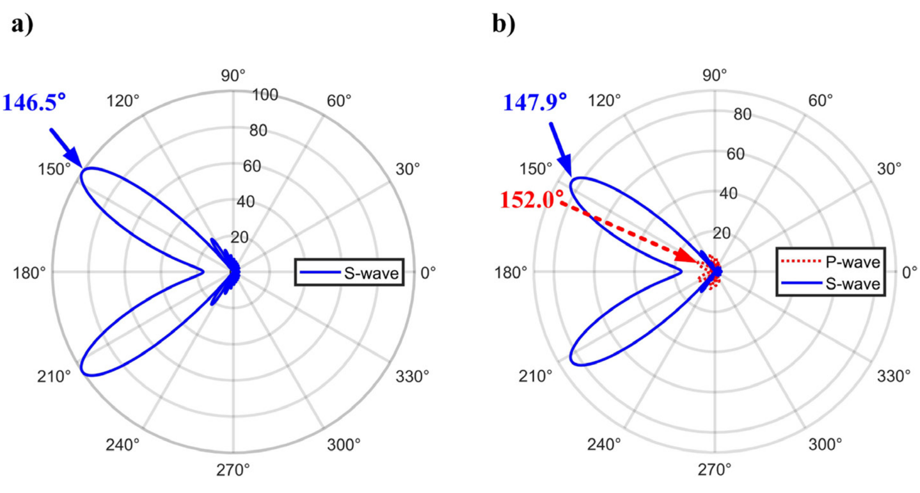

Figure 23. Theoretical radiation patterns after changing the medium density. $d_1 = 2.5$ m, $d_2 = 14.5$ m, $L = 25$ m, $N_t = 8$, $d = 2$ m, $N = 100$, $v_p = 2493$ m/s, $v_s = 1496$ m/s, $v_t = 80$ m/s, and $f = 38.4$ Hz. (a) z-axis section and (b) x-axis section.

DISCUSSION

Small square array data acquisition

To demonstrate the directional characteristics of the seismic wavefield excited by the HST seismic source, we conducted small-scale 3D seismic data acquisition near the Chongqing–Luzhou HSR (a segment of the Chongqing–Kunming HSR). Because deploying receivers in mountainous terrain was impractical, the survey was conducted on the ground. Figure 25a shows the geographical location of the data-acquisition site. Figure 25b shows a photograph of the field deployment, confirming that the HST operated on the ground within the survey area. Figure 25c shows a schematic of the acquisition geometry. A total of 961 receivers were arranged in a 90 m × 90 m square array with 3 m spacing between adjacent sensors. The distance between the railway and square array was 50 m. To facilitate clear visualization of the wavefield snapshots, a coordinate system was established, as shown in Figure 25c, with the coordinates of the four corner receivers explicitly labeled. In addition, a receiver (receiver A in Figure 25c) was deployed adjacent to the HSR to monitor the passage of trains.

During the data observation period, we selected an HST traveling from Chongqing to Luzhou (moving from right to left). The HST consisted of eight carriages and maintained a speed of approximately 93 m/s while passing through the data-acquisition area. The waveform recorded by receiver A (Figure 26a) exhibits a periodicity of 0.27 s, consistent with the theoretical period derived from the HST's structural characteristics and speed (25 m carriage length divided by 93 m/s ≈ 0.269 s). The normalized amplitude spectrum of the HST-excited seismic data recorded by receiver A is shown in Figure 26b, whereas the normalized

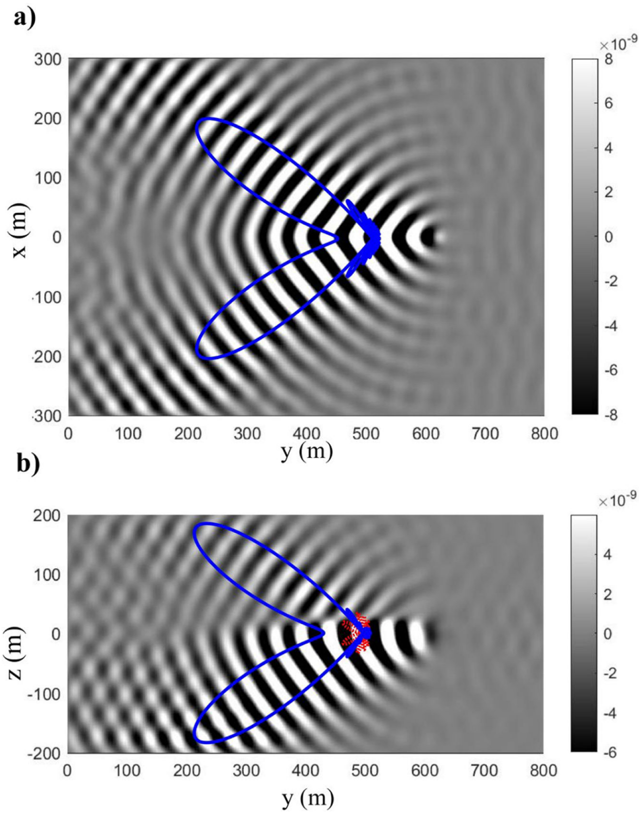

Figure 24. Combined figure of the theoretical radiation patterns and simulated wavefield snapshots after changing the medium density (red lines are the theoretical radiation patterns of P-waves, and blue lines are the theoretical radiation patterns of S-waves). (a) *z*-axis section and (b) *x*-axis section.

average amplitude spectrum from all 961 geophones is displayed in Figure 26c. Both spectra reveal narrowband peaks with a uniform frequency spacing of 3.71 Hz, aligning with the theoretical value calculated from the HST's speed and carriage length (93 m/s divided by 25 m ≈ 3.72 Hz).

The waveform received by receiver A (Figure 26a) indicates that the HST entered the acquisition area at approximately 8.7 s and left at approximately 12.0 s. Given that 26 Hz was a prominent spectral peak in the amplitude spectrum (Figure 26c), we applied filtering to visualize the wavefield of the 26-Hz component. Based on the far-field assumption discussed earlier, we selected two-time instances to display the 26-Hz wavefield snapshots: 3 s before the train entered the acquisition area (i.e., at 5.7 s), as shown in Figures 27a, and 3 s after the train left the acquisition area (i.e., at 15.0 s), as shown in Figure 27b. Both snapshots reveal distinct directional patterns (the approximate propagation directions are indicated by red dashed arrows in the figures). Notably, the propagation angles in the two snapshots are not complementary, further demonstrating that the directional characteristics of seismic wavefields generated by a moving source (including an HST) differ fundamentally from those generated by a fixed-point source.

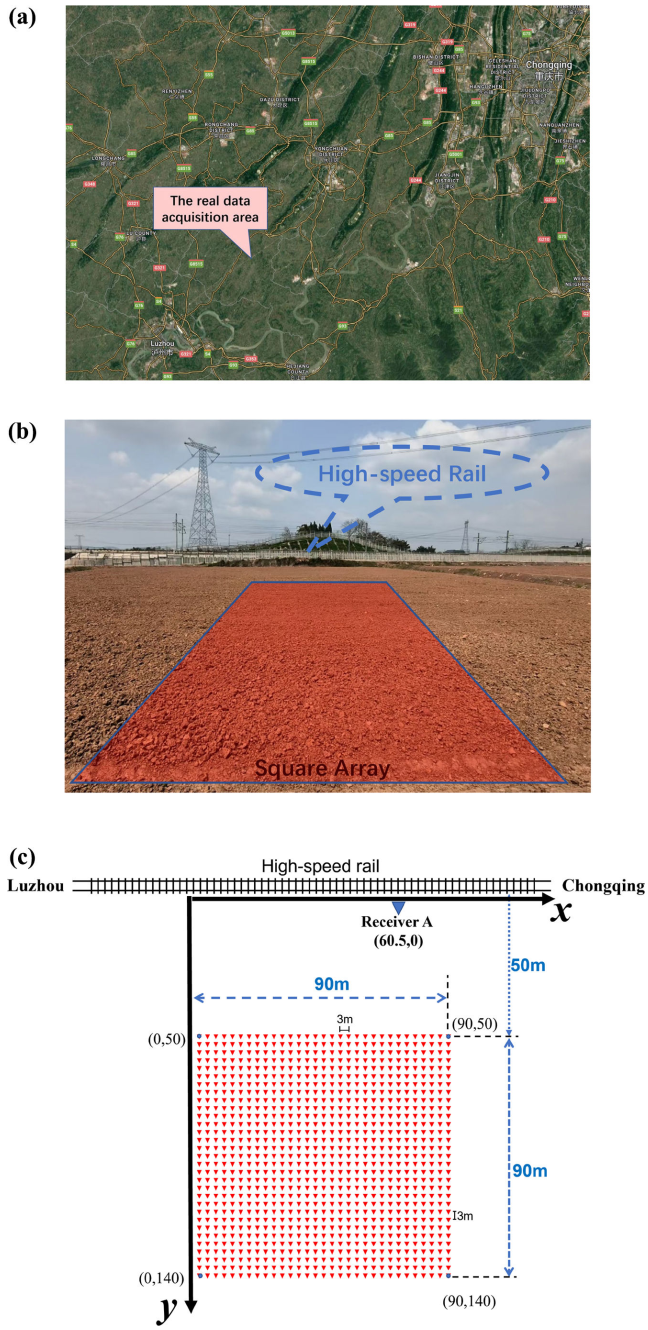

Figure 25. Real data acquisition area near Chongqing–Luzhou high-speed rail and the corresponding acquisition system. (a) Real data acquisition area, (b) a picture taken at the data acquisition site, and (c) schematic diagram of a data acquisition array comprising 961 (31 × 31) receivers.

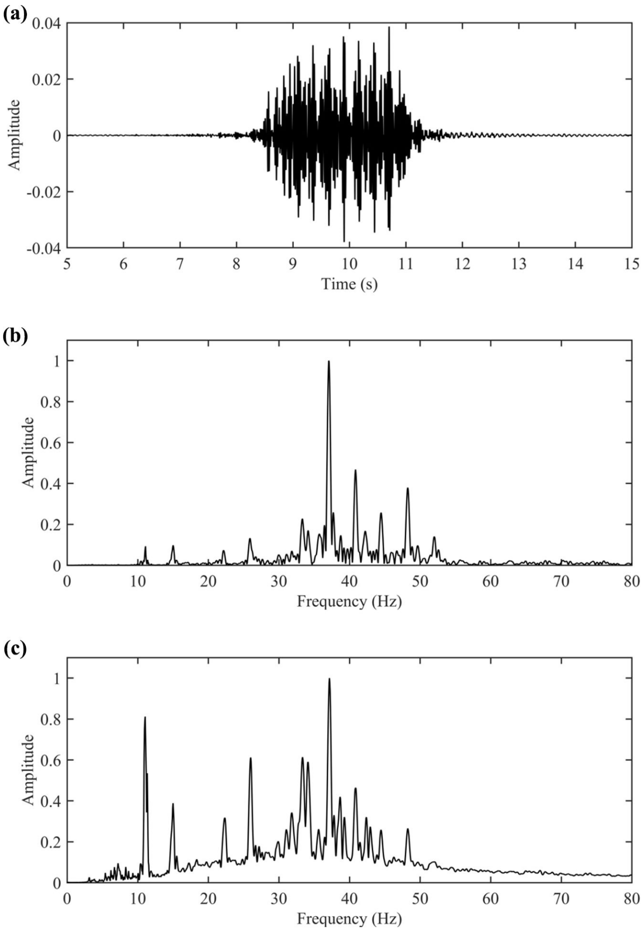

Figure 26. Analysis of data from a high-speed train traveling from Chongqing to Luzhou and passing through the acquisition area. (a) Waveform recorded by receiver A, (b) normalized amplitude spectrum of the seismic data excited by this train and recorded by receiver A, and (c) normalized average amplitude spectrum from all 961 geophones.

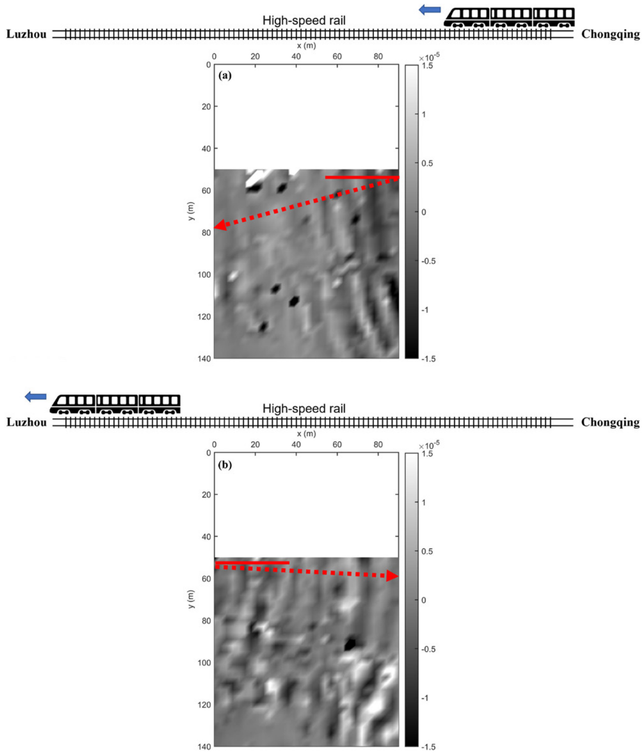

Figure 27. Snapshot of the 26-Hz seismic wavefield excited by a high-speed train. (a) 5.7 s: 3 s before the HST arrived at the acquisition area; (b) 15.0 s: 3 s after the high-speed train left the acquisition area.

Some potential applications

In this section, we provide a prospective outlook for future research based on the results of the previous analysis. Based on equation 21, it can be concluded that when the medium parameters change, the wave velocity in the medium also changes. At an HST speed of 80 m/s, we conducted a comparative analysis after changing only the medium density. The theoretical radiation patterns for different medium densities are shown in Figure 28. As the medium density increased, the intensity of the P-wave interference angle became more pronounced, as shown in the red rose diagrams in Figure 28a–28d. Furthermore, the P-wave interference angle decreased from 156.3° to 144.8° (red rose diagrams in Figure 28b–28d). By contrast, the main lobe of the S-wave interference narrowed (blue rose diagrams in Figure 28), and the S-wave interference angle decreased from 127.7° to 121.2°. These results indicate a clear relation between the medium velocity and the rose-diagram pattern. If a quantitative relation between the medium wave velocity and rose-diagram characteristics (particularly the main lobe angle) can be established, a potential application may emerge; specifically, the approximate medium velocity near the HSR could be inferred for a constant-velocity medium.

The structure and operating speed of HSTs are largely uniform, and HSR parameters, such as sleeper spacing, remain constant. Consequently, the directional characteristics of the seismic wavefields excited by HSTs are relatively stable. Therefore, when acquiring HST-induced seismic data, these stable directional characteristics can be used for illumination analysis, enabling the design of observation systems that yield more reliable seismic wavefields, which may benefit seismic interferometry. With the development of three-component geophones, different types of seismic waves can be retrieved from three-component data sets. Consequently, the directional characteristics of these seismic waves can be further explored.

Conversely, during seismic data acquisition near a high-speed rail, the seismic wavefields induced by HSTs are

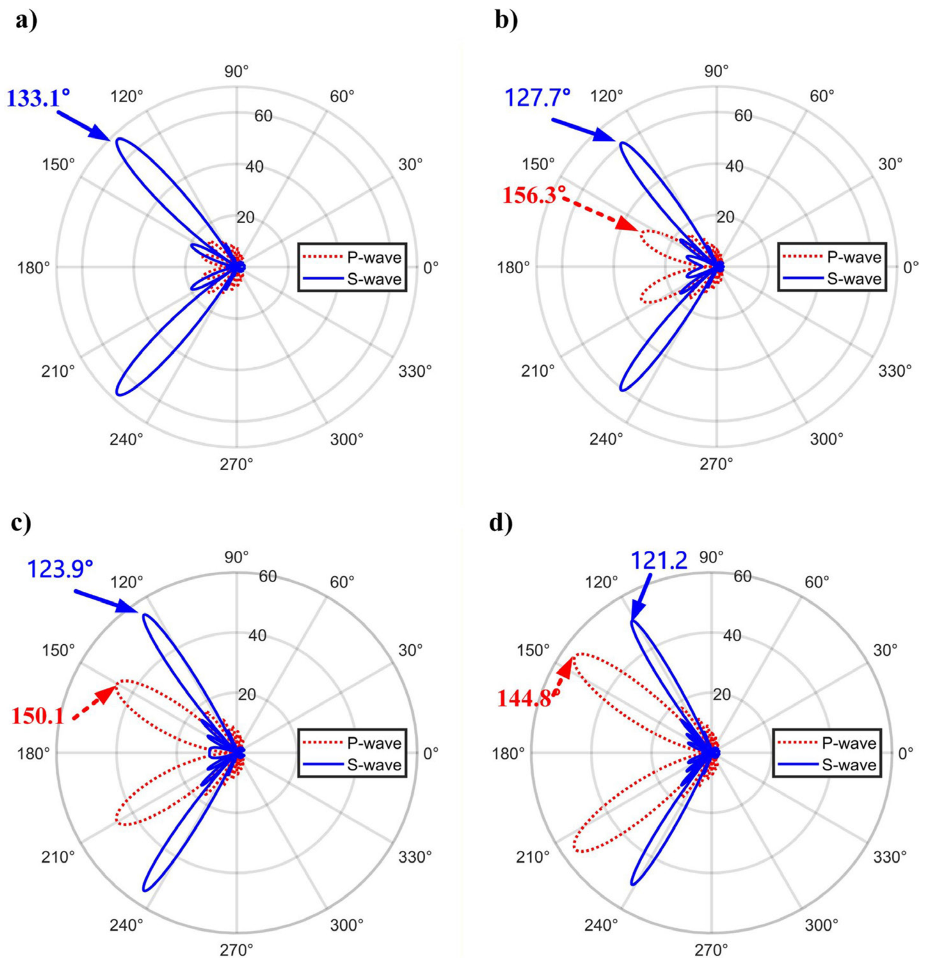

Figure 28. Theoretical radiation patterns at the x-axis section with different medium densities. $d_1 = 2.5\ \mathrm{m}$, $d_2 = 14.5\ \mathrm{m}$, $L = 25\ \mathrm{m}$, $N_t = 8$, $d = 2\ \mathrm{m}$, $N = 100$, $v_t = 80\ \mathrm{m/s}$, and $f = 38.4\ \mathrm{Hz}$. (a) $\rho = 2000\ \mathrm{kg/m^3}(v_p = 2010\mathrm{m/s},\ v_s = 1206\mathrm{m/s})$, (b) $\rho = 2500\ \mathrm{kg/m^3}(v_p = 1798\mathrm{m/s},\ v_s = 1078\mathrm{m/s})$, (c) $\rho = 3000\ \mathrm{kg/m^3}(v_p = 1641\mathrm{m/s},\ v_s = 985\mathrm{m/s})$, and (d) $\rho = 3500\ \mathrm{kg/m^3}(v_p = 1519\mathrm{m/s},\ v_s = 911\mathrm{m/s})$.

generally regarded as noise. However, it may be possible to exploit these directional characteristics to suppress wavefield interference using beamforming.

CONCLUSION

To investigate the characteristics of the seismic wavefields generated by HST sources, we derived a theoretical formula for the directional characteristics of a seismic wavefield excited by HST sources using the theory of uniform linear arrays and seismic wave radiation patterns. In addition, we conducted a parameter analysis of the array factor.

Using the ABAQUS finite element analysis software, we established a model and simulated the seismic wavefield in a tunnel environment. The simulation results reveal distinct interference phenomena. When the speed of the HST was changed, the main lobe of the seismic wavefield interference changed accordingly.

To validate the derived theoretical formula, we combined the theoretical radiation patterns with simulated wavefields. From the combined diagrams, we observed strong consistency between the theoretical radiation patterns and main interference lobes of the simulated wavefield. This conclusion remains valid when we change the HST speed or medium parameters.

Although this study focused on the directional characteristics of the seismic wavefields generated by HSTs on traditional sleeper-supported tracks, the proposed theoretical framework is likely to be extendable to the analysis of wavefield directivity in viaduct-based high-speed rail systems.

ACKNOWLEDGMENTS

This work was supported in part by the National Key Research and Development Program of China under grant number 2021YFA0716904, in part by the National Natural Science Foundation of China under grant numbers 41974131 and 42374153, in part by the Fundamental Research Funds for the Central Universities under grant number xzy012023073, and in part by the Innovation Capability Support Program of Shaanxi under grant number 2021TD-08. The authors would like to thank BGP Inc., China National Petroleum Corporation for providing real data in the discussion part.

DATA AND MATERIALS AVAILABILITY

Data associated with this research are confidential and cannot be released.

REFERENCES

Chen, J., and J. Cao, 2020, Green's function for three-dimensional elastic wave equation with a moving point source on the free surface with applications: Geophysical Prospecting, **68**, no. 4, 1281–1290, doi: 10.1111/1365-2478.12928.

Chen, Y., and H. Gu, 2023, Theoretical foundations of seismic sources. Science Press: Beijing, China.

Frýba, L., 2001, A rough assessment of railway bridges for high speed trains: Engineering Structures, **23**, no. 5, 548–556, doi: 10.1016/S0141-0296(00)00057-2.

Fuchs, F., G. Bokelmann, and the AlpArray Working Group, 2018, Equidistant spectral lines in train vibrations: Seismological Research Letters, **89**, no. 1, 56–66, doi: 10.1785/0220170092.

Gao, G., S. Yao, J. Yang, and J. Chen, 2019, Investigating ground vibration induced by moving train loads on unsaturated ground using 2.5D FEM: Soil Dynamics and Earthquake Engineering, **124**, 72–85, doi: 10.1016/j.soildyn.2019.05.034.

Halliday, D., A. Curtis, and E. Kragh, 2008, Seismic surface waves in a suburban environment: Active and passive interferometric methods: The Leading Edge, **27**, no. 2, 210–218, doi: 10.1190/1.2840369.

Hu, G., G. Zhang, S. Sun, Y. Li, J. Yang, J. Duan, H. He, et al, 2019, FWI of high-speed-train seismic first arrival signal: Chinese Journal of Geophysics, **62**, no. 12, 4817–4824, doi: 10.6038/cjg2019N0163.

Jiang, Y., J. Ning, J. Wen, and Y. Shi, 2022, Doppler effect in high-speed rail seismic wavefield and its application: Science China Earth Sciences, **65**, no. 3, 414–425, doi: 10.1007/s11430-021-9843-0.

Lavoué, F., O. Coutant, P. Boué, L. Pinzon-Rincon, F. Brenguier, R. Brossier, P. Dales, M. Rezaeifar, et al, 2021, Understanding seismic waves generated by train traffic via modeling: Implications for seismic imaging and monitoring: Seismological Research Letters, **92**, no. 1, 287–300, doi: 10.1785/0220200133.

Liu, L., and Y. Jiang, 2019, Attribution extraction and feature analysis for large amount of high-speed-train seismic events: Chinese Journal of Geophysics, **62**, no. 6, 2313–2320, doi: 10.6038/cjg2019M0682.

Liu, Y., Y. Yue, Y. Li, and Y. Luo, 2022, On the retrievability of seismic waves from high-speed-train-induced vibrations using seismic interferometry: IEEE Geoscience and Remote Sensing Letters, **19**, 1–5, doi: 10.1109/LGRS.2021.3050205.

Liu, Y., Y. Yue, Y. Luo, and Y. Li, 2021, The seismic broad-band signature of high-speed trains running on viaducts: Geophysical Journal International, **226**, no. 2, 884–892, doi: 10.1093/gji/ggab144.

Luo, J., X. Wang, and W. Chen, 2022, Subsurface elastic parameter reconstruction based on seismic data from the high-speed trains using full waveform inversion: IEEE Transactions on Geoscience and Remote Sensing, **60**, 1–8, doi: 10.1109/TGRS.2022.3151352.

Luo, J., X. Wang, and W. Chen, 2023, Imaging the subsurface with the high-speed train seismic data-based elastic reverse time migration: IEEE Transactions on Geoscience and Remote Sensing, **61**, 1–9, doi: 10.1109/TGRS.2023.3306013.

Mi, B., J. Xia, Y. Xu, B. You, and Y. Chen, 2023, Retrieval of surface waves from high-speed-train-induced vibrations using seismic interferometry: Geophysics, **88**, no. 5, KS113–KS126, doi: 10.1190/geo2022-0603.1.

O'Brien, J., and D. C. Rizos, 2005, A 3D BEM-FEM methodology for simulation of high-speed train induced vibrations: Soil Dynamics and Earthquake Engineering, **25**, no. 4, 289–301, doi: 10.1016/j.soildyn.2005.02.003.

Shao, J., Y. Wang, and L. Chen, 2022, Near-surface characterization using high-speed train seismic data recorded by a distributed acoustic sensing array: IEEE Transactions on Geoscience and Remote Sensing, **60**, 1–11, doi: 10.1109/TGRS.2022.3153831.

Shi, Y., J. Wen, and J. Ning, 2022, Theoretical analysis of high-speed rail seismic imaging: Science China Earth Sciences, **65**, no. 4, 714–723, doi: 10.1007/s11430-021-9840-x.

Takemiya, H., and X. Bian, 2005, Substructure simulation of inhomogeneous track and layered ground dynamic interaction under train passage: Journal of Engineering Mechanics, **131**, no. 7, 699–711, doi: 10.1061/(ASCE)0733-9399(2005)131:7(699).

Takemiya, H., and X. Bian, 2007, Shinkansen high-speed train induced ground vibrations in view of viaduct–ground interaction: Soil Dynamics and Earthquake Engineering, **27**, no. 6, 506–520, doi: 10.1016/j.soildyn.2006.11.003.

Wang, Y., 2015, Frequencies of the Ricker wavelet: Geophysics, **80**, no. 2, A31–A37, doi: 10.1190/geo2014-0441.1.

Wang, H., and J. Chen, 2023, Wavefield modeling and characteristic analysis for a uniformly moving high-speed-train source under a two-layered model with applications: IEEE Transactions on Geoscience and Remote Sensing, **61**, 1–14, doi: 10.1109/TGRS.2023.3318252.

Wang, Z., C. Chen, W. Bai, and Y. Li, 2022, Analysis of the responses of seismic waves excited by the pile foundations of the viaduct when the high-speed trains passage: Chinese Journal of Geophysics, **65**, no. 7, 2622–2635, doi: 10.6038/cjg2022P0297.

Wang, X., W. Chen, J. Wen, J. Ning, and J. Li, 2019, The applications of synchrosqueezing time-frequency analysis in high-speed train induced seismic data processing: Chinese Journal of Geophysics, **62**, no. 6, 2328–2335, doi: 10.6038/cjg2019M0658.

Wang, Z., Y. Li, and W. Bai, 2020, Numerical modelling of exciting seismic waves for a simplified bridge pier model under high-speed train passage over the viaduct: Chinese Journal of Geophysics, **63**, no. 12, 4473–4484, doi: 10.6038/cjg2020O0156.

Wang, X., X. Pan, J. Luo, W. Chen, and B. Wang, 2024a, Forward modeling of seismic wavefield induced by the high-speed trains in three-dimensional space: IEEE Transactions on Geoscience and Remote Sensing, **62**, 1–11, doi: 10.1109/TGRS.2024.3420931.

Wang, X., B. Wang, and W. Chen, 2021, The second-order synchrosqueezing continuous wavelet transform and its application in the high-speed-train induced seismic signal: IEEE Geoscience and Remote Sensing Letters, **18**, no. 6, 1109–1113, doi: 10.1109/LGRS.2020.2993596.

Wang, X., S. Xia, X. Pan, B. Wang, D. Liu, and W. Chen, 2024b, The broadband virtual shot gathers construction based on high-speed train-induced seismic wave: IEEE Transactions on Geoscience and Remote Sensing, **62**, 1–12, doi: 10.1109/TGRS.2024.3481272.

Wen, J., J. Ning, and X. Zhang, 2019, Theoretical analysis on the characteristics of seismic wave field produced by high-speed train: Acta Scientiarum Naturalium Universitatis Pekinensis, **55**, no. 5, 813–822, doi: 10.13209/j.0479-8023.2019.074.

Xia, S., X. Wang, W. Chen, X. Pan, and J. Luo, 2025, Extracting dispersion spectrum directly from the high-speed train-induced seismic signal: IEEE Geoscience and Remote Sensing Letters, **22**, 1–5, doi: 10.1109/LGRS.2024.3509134.

Xu, G., and H. Zhou, 1982, Principles of seismology. Science Press: Beijing, China.

Yin, C., Y. Shi, H. Wu, J. Wen, and J. Ning, 2024, Theoretical analysis of generating virtual seismic gatherings through high-speed rail-induced subsurface seismic wave fields: Chinese Journal of Geophysics, **67**, no. 1, 251–260, doi: 10.6038/cjg2023P0377.

Zhang, G., C. He, Y. Li, J. Duan, T. Wang, Y. Zhan, H. Du, et al, 2019, Wavelet time function of high-speed-train seismic source and verification: Chinese Journal of Geophysics, **62**, no. 6, 2344–2354, doi: 10.6038/cjg2019M0661.

Zhang, H., B. Wang, J. Ning, and Y. Li, 2019, Interferometry imaging using high-speed-train induced seismic waves: Chinese Journal of Geophysics, **62**, no. 6, 2321–2327, doi: 10.6038/cjg2019M0676.

Zhou, N., W. Chen, J. Luo, and X. Wang, 2024, Elastic wave equation traveltime inversion with dynamic time warping based on high-speed train seismic data: IEEE Transactions on Geoscience and Remote Sensing, **62**, 1–11, doi: 10.1109/TGRS.2024.3397813.mology.

Biographies and photographs of the authors are not available.